Laser and Particle Beams

cambridge.org/lpb

Flux and estimated spectra from a low-intensity laser-driven X-ray source

L. Tyler Mix, James A. Maslow, Michael A. Jaworski and Joshua E. Coleman

Los Alamos National Laboratory, Los Alamos, NM, USA

Research Article

Cite this article: Mix LT, Maslow JA, Jaworski MA, Coleman JE (2024) Flux and estimated spectra from a low-intensity laser-driven X-ray source. *Laser and Particle Beams* **42**, e1, 1–9. https://doi.org/10.1017/lpb.2024.1

Received: 18 October 2023
Accepted: 5 February 2024

Keywords:
diamond radiation detectors; foil hydrodynamics; hydrodynamic simulations; KeV X-rays; laser-driven X-rays; X-ray spectra

Corresponding author: L. Tyler Mix;
Email: ltmix@lanl.gov

Abstract

Laser-driven X-rays as probes for high-energy-density physics spans an extremely large parameter space with laser intensities varying by 8 orders of magnitude. We have built and characterized a soft X-ray source driven by a modest intensity laser of 4×10^{13} W/cm^2. Emitted X-rays were measured by diamond radiation detectors and a filtered soft X-ray camera. A material-dependence study on Al, Ti, stainless steel alloy 304, Fe, Cu and Sn targets indicated 5-μm-thick Cu foils produced the highest X-ray yield. X-ray emission in the laser direction and emission in the reverse direction depend strongly on the foil material and the thickness due to the opacity and hydrodynamic disassembly time. The time-varying X-ray signals are used to measure the material thinning rate and is found to be ∼1.5 μm/ns for the materials tested implying thermal temperature around 0.6 eV. The X-ray spectra from Cu targets peaks at ∼2 keV with no emission >4 keV and was estimated using images with eight different foil filters. One-dimensional hydrodynamic and spectral calculations using HELIOS-CR provide qualitative agreement with experimental results. Modest intensity lasers can be an excellent source for nanosecond bursts of soft X-rays.

Introduction

Laser-produced plasmas have been studied as a source of X-ray radiation since the very early days of the laser (Ref. 1). The field has advanced largely to address two related goals: laser-driven inertial confinement fusion and laser-produced X-ray probes. To achieve those goals, a signification portion of laser X-ray generation research was performed at large facilities such as Shiva (Ref. 2), Argus (Ref. 2), Nova (Refs 3, 4), J-KAREN (Ref. 5) and Trident (Ref. 6), with ongoing experiments at NIF, (Refs 7, 8) OMEGA (Refs 3, 9), ALEPH (Ref. 10), ELI-NP (Ref. 11), SULF (Ref. 12) and many others. These laser systems typically operate with either kJ-class ns beams at $\sim 10^{16}$ W/cm^2, or 1–100 J-class ultrashort beams with intensities of $\sim 10^{20-21}$ W/cm^2. In comparison, experiments with J-class ns lasers with intensities of $\sim 10^{13}$ W/cm^2 are a less explored area of laser–plasma interactions. However, modest laser intensities hold promise for their significant X-ray yield in the 1–5 keV range which can be used for biological imaging (Ref. 13) and detector calibration (Ref. 14).

Intense laser radiation on a metal foil ablates the material, forming a solid density plasma. Depending on the laser intensity, thickness of the foil and the hydrodynamic disassembly process, a portion of the foil remains intact while the laser pulse heats the plasma formed on the front surface. For ns class lasers $<10^{15}$ W/cm^2, inverse bremsstrahlung is the dominant mechanism of laser absorption (Ref. 15). Laser energy is absorbed by the electrons most efficiently at densities with $n_e < n_c$, where the critical density is $n_c = 3.9 \times 10^{21}$ cm^{-3} for 532 nm radiation (Ref. 16). At greater densities, the plasma becomes opaque, and these plasma regions are heated by thermal conduction of the hot electrons (Ref. 17). After the plasma is sufficiently hot, it radiates the absorbed energy out as bremsstrahlung X-rays and line spectra from the highly ionized metal atoms. Inner shell ionization of cold atoms to produce K-line emission generally requires much higher laser intensities and hotter election populations. The opacity of the plasma and condition of the foil heavily influence the transport of X-ray radiation to the sample and detectors (Ref. 15).

Marzi et al. (Ref. 13) and Labate et al. (Refs 14, 18, 19) describe a laser-driven soft X-ray source for both biomedical imaging applications and CCD camera calibration. They use a single beam of 3-J, 3-ns Full Width Half Max (FWHM), 1053-nm pulse for an intensity of 5×10^{12} W/cm^2, incident upon a solid cylinder target. Cu produced the highest yield of 1–5 keV X-rays when compared with plexiglass, Al, Mo and W (Ref. 13). Years prior, Eidmann and Kishimoto (Ref. 20) measured X-ray spectra from 50 eV to 1.2 keV with a 7-J, 3-ns (FWHM), 532-nm pulse for an intensity of 3×10^{13} W/cm^2 with flat solid targets. Their results from Be, C, Al, Ti, Cu, Mo, Sn, W, Au and Pb also identified Cu with the highest intensity X-ray emissions (Ref. 20). Near 1 keV, the spectrum for Cu was dominated by L-shell emission. More recent work on Al, Cu and

© The Author(s) 2024. Published by Cambridge University Press. This is an Open Access article, distributed under the terms of the Creative Commons Attribution licence (http://creativecommons.org/licenses/by/4.0), which permits unrestricted re-use, distribution and reproduction, provided the original article is properly cited.

Au by Chaurasia et al. (Refs 21–23), using a single 2- to 15-J, 500-ps, 1064-nm pulse for a maximum intensity of 4×10^{14} W/cm^2 on target, described the variation of X-ray emission with focal position and thus the spot size. Shots that were slightly out of focus produced larger signals of soft X-rays (0.7–1.5 keV) from the larger volume of plasma. Shots that were in focus produced more emission of harder X-rays (3–5 keV). Gaeta et al. (Ref. 24) expanded a low-energy laser X-ray source to four beam lines of 2.8×10^{14} W/cm^2 each with a 37-μm-thick copper tape target to produce ∼1 keV radiation for lithography applications at 300 Hz for 3.8 W/sr average power. They concluded that a laser system with a moderate energy and a small focal spot and short pulse width produces X-rays at a higher efficiency than systems with similar intensities and larger energy per pulse (Ref. 24).

We have begun developing a similar laser-driven benchtop X-ray source for detector and diagnostic development at the Dual Axis Radiographic Hydrodynamic Test (DARHT) Facility (Ref. 25). In comparison to previous work, our laser system uses thin (2.5–10.0 μm) foils with a 5-J, 8-ns, 532-nm pulse and an intensity of 4×10^{13} W/cm^2. Our primary goal is to calibrate a suite of X-ray detectors and spectrometers before installation on DARHT. In this work, we detail initial experiments with multiple foil materials and thicknesses on the DARHT soft X-ray test stand to understand and commission this X-ray source to complement the future Bragg crystal spectrometer calibrations.

Materials and methods

The simple goal of the experimental apparatus (Fig. 1) is to put the most intense photon beam possible onto the metal foil target and detect the generated X-rays. The optical beam is produced in a flashlamp-pumped Nd:YAG (Ref. 26) and frequency doubled to 532 nm with a maximum energy of ∼5 J per 8-ns (FWHM) pulse. The beam is focused onto the foil with a 150-mm lens to a 1/e^2 diameter of ∼40 μm; providing an intensity of 4×10^{13} W/cm^2. The focal spot size was limited by experimental factors to protect the optics from metal debris. A photodiode (Ref. 27) monitors the scattered laser light from an alignment mirror and is calibrated to provide the laser energy on every shot. The foils are mounted on an aluminum frame inside the target chamber at 10^{-7} Torr with a manipulator arm to move a new sample into the target position for each shot.

Diamond radiation detectors (DRDs), which are most sensitive to X-rays <6 keV and have an instrument response time of ∼200 ps, are the main detectors for the emitted X-rays (Refs 28–31). These detectors are 3 × 1 × 1 mm and are mounted on an SMA connector that provides a −150 V bias and records the induced current. The DRDs on the right of Fig. 1 pointed at the front of the target surface measure the X-rays in the 'backward direction' and the DRDs on the left behind the target measure the X-rays in the 'forward direction', which we define here for the remainder of this work. The DRDs were cross calibrated, corrected for non-linearity in high-voltage signals and the signals compared here are using DRDs of the same size from the same manufacturer. Coarse X-ray spectroscopy measurements were made using eight different metal filters mounted to an anodized Al base and the Sophia-XO camera (Ref. 32). The camera has a square 2048 pixel array with square 13.5-μm pixels and a 200-μm-thick silicon sensor. The Sophia has a quantum efficiency >60% for X-rays between 0.5 and 5.0 keV (Supplemental Figure S1). The camera sensor was overexposed for 100 ns, integrating the entire X-ray pulse. Light-tight filters on both the DRDs and the Sophia camera are 500 ± 5 nm of Al on top of a 5 ± 0.25-μm polyimide support (Ref. 33). Thicker Al filters of 50 and 300 μm were used for higher energy X-ray measurements on two additional DRDs. Targets for this initial study included 10-μm-thick Al, Ti, stainless steel alloy number 304 (SS-304), Fe, Cu and Sn (Ref. 34). Also, 2.5- and 5-μm-thick foils of Ti, Fe and Cu were also shot to quantify the thickness dependence on X-ray yield.

Results and discussion

Time-resolved X-ray measurements

We performed a series of time-resolved X-ray measurements using DRDs with different foils at laser intensities from 0.8×10^{13} to

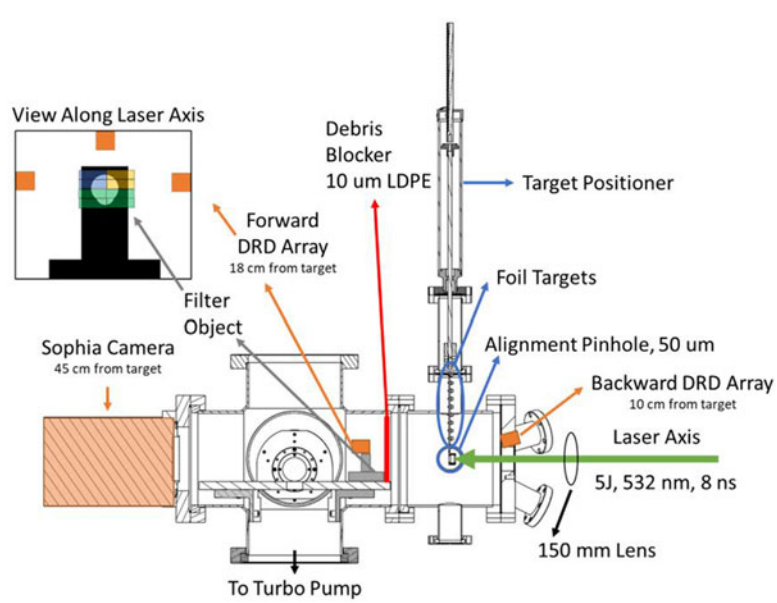

Figure 1. The laser beam enters the target chamber from the right striking the metal foil in the center. A group of DRDs is mounted facing the target front to detect backscattered radiation with different Al filters 10 cm from the target. A second group of DRDs is mounted around the filter object to detect forward-scattered radiation 18 cm from the target. The Sophia camera is mounted at the end of the chamber 45 cm from the target.

https://doi.org/10.1017/lpb.2024.1 Published online by Cambridge University Press

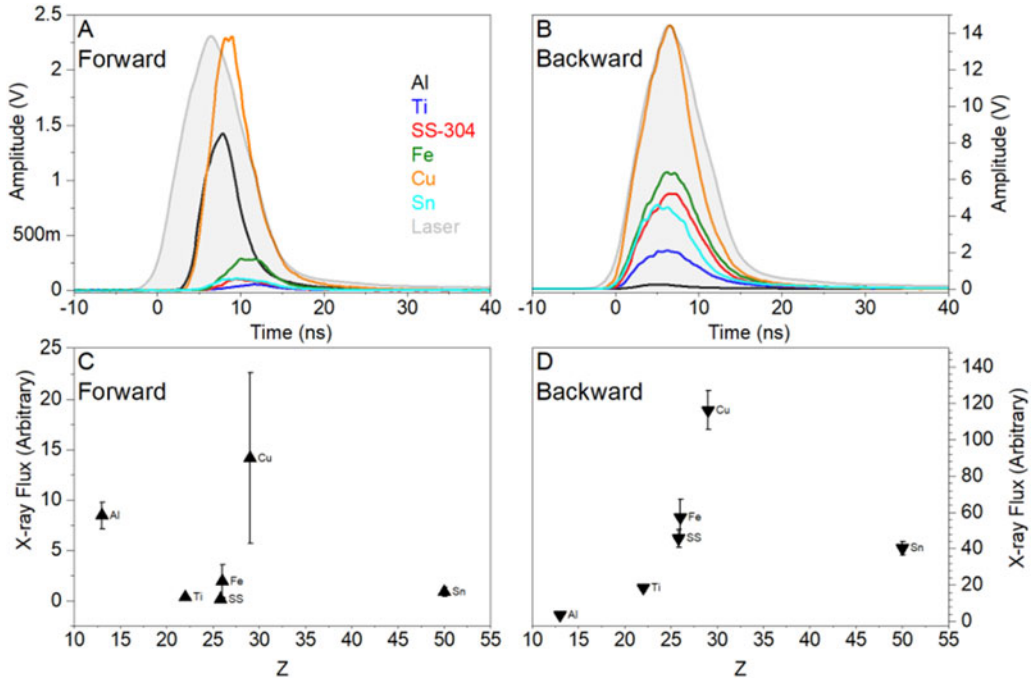

Figure 2. (A) Average DRD X-ray signals from up to 15 shots in the forward direction for Al, Ti, SS-304, Fe, Cu and Sn. (B) Average signals in the backward direction. The laser pulse is shown in grey and scaled for easy comparison. (C) Average numerically integrated signal for each material over five shots in the forward direction. (D) Average numerically integrated signals in the backward direction.

4.0×10^{13} W/cm^2. Figure 2A shows the average DRD signals of the forward-scattered X-rays from each material for up to 15 shots with 4×10^{13} W/cm^2 of laser intensity. Time zero in these and all other figures in this paper is set when 10% of the peak of the laser pulse arrives at the foil. Cu targets yield the brightest X-ray source, at the expense of larger shot-to-shot variation. Al generates much larger X-ray signals than the other higher Z materials, aside from Cu, in the forward direction. In the backward direction, Fig. 2B, Cu remains the strongest emitter. Al is the weakest X-ray emitter in the backward direction.

The average integrated signal versus atomic number Z is plotted in Fig. 2C, where there is not a clear dependence on Z for the forward-scattered X-rays. The expected increase in X-ray yield due to the Z^2 scaling of the inverse bremsstrahlung absorption coefficient (Ref. 15) is evident in the integrated back-scattered X-ray flux, shown in Fig. 2D. Cu has the best combination of a high Z number for efficient absorption of laser energy by inverse bremsstrahlung and low ionization energies, allowing a large fraction of the plasma to ionize to the K and L shells which then emit keV X-ray radiation (Ref. 13). Ti has lower ionization energies and would have a larger fraction of K and L shell ionization; however, it does not absorb the laser energy as efficiently. Sn exhibits the opposite phenomenon. It has a high Z and absorbs the laser energy strongly but has much higher ionization energies and much smaller fractions of K and L shell ionized atoms. Sn plasmas would be expected to have large fractions of M shell ions which emit in the extreme ultraviolet region and is blocked by the light filters on our DRDs. Similar trends were observed by Marzi (Ref. 13), Eidmann (Ref. 20) and Chaurasia (Ref. 22) who all found Cu had the largest X-ray yield with laser intensities near 10^{13} W/cm^2.

The large differences in X-ray emittance and timing in the forward- and back-scattered directions (Fig. 2) are an effect of the hydrodynamic disassembly time and the opacity of the foil before disassembly. The forward-scattered X-rays arrive at the DRDs between 3.7 and 6.3 ns after the laser hits the foil. In the backward direction, the X-rays arrive between 0.5 and 0.9 ns after the laser pulse which is slightly longer than the 0.3 ns (10 cm) transit time for light from the plasma to the DRD array. Based on the X-ray arrival times, Al, Cu and Sn disassemble faster than the Ti, Fe and SS-304.

With detectors in both the forward and backward directions, an attenuation study was performed. Using the transmission equation, it is possible to calculate the time-dependent thickness of the foil and the speed of the ablation or hydrodynamic disassembly process.

$$\frac{I_{\mathrm{For}}}{I_{\mathrm{Back}}}(t) = \mathrm{e}^{-\frac{\mu}{\rho}\rho z(t)} \tag{1}$$

where I_{For} is the forward DRD signal transiting the foil corrected for distance, I_{Back} is the backward DRD signal corrected for distance, μ/ρ is the mass attenuation coefficient (Ref. 35), ρ is the material density and $z(t)$ is the foil thickness. Signal intensity was corrected for the distance traveled using the inverse-square law. We believed that the X-ray radiation source was created by the laser on the front surface of the foil and the source radiates outwards isotropically into 4π steradians (sr) and the X-rays either transit the foil or are absorbed by the foil. There is no reflection. Mass attenuation coefficients depend on energy, and we have selected to use the values at 2 keV, the peak of the estimated Cu X-ray spectrum, as described below.

The Cu foil is initially 10 μm thick and has begun thinning when the first signals are detectable above the noise by the forward DRD (Fig. 3). A 10-μm-thick copper foil attenuates 2 keV X-rays by 10^{-6}, while 5-μm-thick Cu foils attenuate by 10^{-4} where signals are first observed in the forward direction. The foil thickness over time

https://doi.org/10.1017/lpb.2024.1 Published online by Cambridge University Press

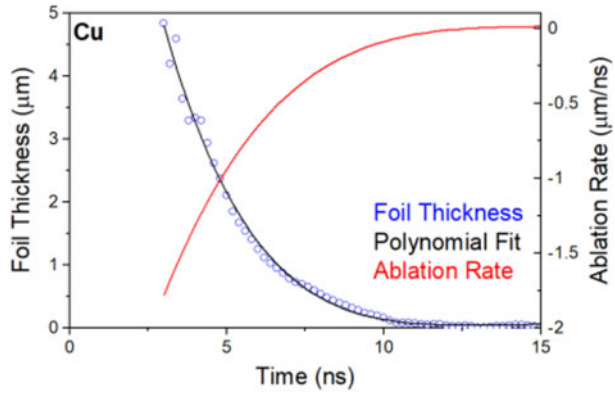

Figure 3. Ablation rate for 10-μm-thick Cu foils. A fifth-order polynomial fit (black) to the thickness data (blue) was used to calculate the ablation rate, d*z*/d*t* (red). The maximum ablation rate is 1.78 μm/ns.

was fitted to a fifth-order polynomial to provide a smooth function to calculate the ablation rate, d*z*/d*t*. Ablation rate has an average rate of 0.65 μm/ns and an instantaneous maximum of 1.78 μm/ns early in time. This speed is faster than the Maxwell–Boltzmann root mean squared speed of 1.05 μm/ns for a distribution of gaseous Cu at the boiling point (2835 K) and slower than the solid Cu bulk speed of sound, 3.75 μm/ns. Similar calculations were performed for Cu of 5 and 2.5 μm thick and different laser intensities. The slight trend towards faster ablation rates with more laser energy is encouraging; however, given the large uncertainties from shot to shot variation, measurement error with small signals, and the spectral estimation we do not believe these differences are meaningful. Cu, Ti, Fe and Sn samples with a thickness of 10 μm (Supplemental Figure S2) and the ablation speeds are compared in Table 1. If the rates were completely driven by the boiling material, we would expect a scaling with the square root of the atomic mass. These rates do not follow that trend. If the measured ablation speeds do represent the root mean squared velocity of the atoms, it implies a temperature for the sublimating atomic Cu material around 6900 K or 0.6 eV. This is not the electron plasma temperature that creates the bremsstrahlung X-rays. Simulations predict a maximum plasma temperature of ∼800 eV as described below. The ablation rates are a subject of ongoing study and research.

We examined the effect of foil thickness on the X-ray intensity in the forward direction; a thinner foil has a shorter absorbance path length and disassembles faster, so it should produce stronger X-rays in the forward direction. We observed a slight increase in the percentage of forward-scattered X-rays with thinner foils shown in Fig. 4. The absolute magnitude of the observed X-rays was highest with 5-μm foils for Ti and Fe and with 2.5-μm foils for Cu. The drop in X-ray flux from 2.5-μm foils is likely due to a smaller plasma volume, thus producing less radiation. This is verified by a similar decrease in radiation in the backscattered direction for 2.5-μm foils versus 5-μm foils, along with Chaurasia's (Ref. 22) measurements that smaller plasma volumes produce less X-rays. In Cu, the improvement in the percentage of forward-scattered X-ray transmission for the 2.5-μm foil was large enough to offset the decreased radiation production. The timing of the arrival of the X-ray pulse at the DRDs is also shortened with thinner foils (Supplemental Figure S3) which is consistent with the ablation rates.

Filtered X-ray spectral estimation

Spectra of the emitted X-rays from Cu were estimated by using eight different foil filters imaged onto the Sophia camera as shown in Fig. 5A. The transmission of each of these filters, shown in Fig. 5B, is calculated from the Center for X-ray Optics online database (Refs 36, 37). To extract the estimated spectra, we employed an expectation–maximization method, used for medical computed tomography images (Refs 38, 39). This method uses an estimate of the spectra, calculates the expected signal amplitude with each filter, compares the expected signal to the actual signal and adjusts the spectral estimate. We used a 400 eV blackbody spectral guess with additional Cu K-alpha lines that was both wider and more intense than the actual spectra as required by the expectation maximization algorithm. Approximately 100 iterations are required to arrive at an estimated spectra that accurately reproduces the measured signal for each filter within a 10% error. Spectra were smoothed via a Gaussian basis set of 200 functions.

Table 1. Ablation rates

Material	Density (g/cm^3)	*Z* Number	Max. Ablation Rate (μm/ns)[a]	Temperature (K)
Al	2.700	13	–	–
Ti	4.507	22	0.90	1550
SS-304	8.000	25.8[b]	–	–
Fe	7.874	26	1.05	2470
Cu (10 μm, 4.0 × 10^{13} W/cm^2)			1.78	8070
Cu (5 μm, 4.0 × 10^{13} W/cm^2)			1.55	6120
Cu (2.5 μm, 4.0 × 10^{13} W/cm^2)	8.960	29	1.68	7190
Cu (5 μm, 1.6 × 10^{13} W/cm^2)			1.58	6360
Cu (5 μm, 2.4 × 10^{13} W/cm^2)			1.62	6685
Cu (5 μm, 3.2 × 10^{13} W/cm^2)			1.67	7105
Average			1.64 ± 0.07	6900 ± 640
Sn	7.310	50	1.03	5000

[a]Al and SS-304 rates were not calculated.
[b]Weighted average of the alloy.

https://doi.org/10.1017/lpb.2024.1 Published online by Cambridge University Press

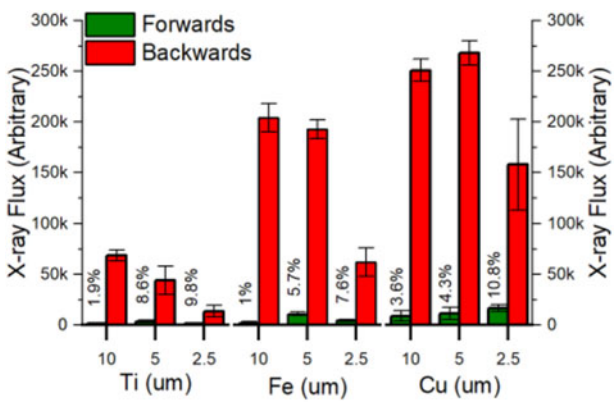

Figure 4. Average numerically integrated DRD X-ray signals for five shots in the forward (green) and backward (red) direction for 10-, 5- and 2.5-μm-thick targets of different materials. The percentage of the flux in the forward direction relative to the flux in the backward direction is given.

The calculated spectra from 5 μm Cu targets at different laser intensities are shown in Fig. 6. The intensity setting was adjusted by lowering the laser output energy, keeping the spot size fixed. These spectra show an increase in amplitude with increasing laser intensity and a slight shift in the peak to higher energy emission from 1.7 to 1.9 keV. There is no evidence of emission at the Cu K-lines at 8.047, 8.027 and 8.905 keV or H and He-like lines near 8.666, 8.699, 8.347 and 8.392 keV (Ref. 37). Cu K-alpha and K-beta lines were inserted into the initial spectral guess and are significantly reduced by the iterative algorithm. Omitting these spectral lines from the initial guess results in negligible change in the spectra <4 keV, and no signal >4 keV (Supplemental Figure S4). Additional measurements from DRDs with 50-μm Al filters, which have <1% transmission <3.5 keV and >50% transmission >7.8 keV, only recorded noise, further supporting that Cu K-line radiation is not produced (Supplemental Figure S5). It is possible that emission from the Cu L-lines at ∼900 eV and lines from Li-like ions at 1.3–2.6 keV, Ne-like ions at 1–1.5 keV and F-like ions at 1–1.2 keV (Ref. 40) are not being resolved with this coarse spectral measurement technique (Ref. 37).

The estimated spectra have several features which are artifacts of the spectral estimation method due to the strong absorption edges in the available metal filters. At the low end of the spectra, we would expect the decline to be smooth, and the estimated peak at 500 eV is a result of the Ti L absorption edge in the same spectral range. The sharp discontinuities at 5 and 7 keV are from the Ti K-edge and the Fe K-edge.

Simulations

Hydrodynamic simulations were performed using the one-dimensional (1-D) radiation-magneto-hydrodynamic software HELIOS-CR (Ref. 41). HELIOS-CR utilized Lagrangian methods to solve conservation equations, frequently used in the inertial confinement fusion community for laser-produced plasma (Ref. 42) and Z-pinch plasma simulations (Ref. 43). HELIOS-CR simulations were performed using a 5-J, 10-ns (FWHM), 532-nm pulse with a 40 μm spot size resulting in an intensity of 4×10^{13} W/cm^2 incident on 10-, 5- and 2.5-μm-thick foils of Al, Ti, Fe and Cu. The foils are divided into 100 zones of equal size, which are 0.1, 0.05 and 0.025 μm thick depending on the foil. The provided PROPACEOS (Ref. 41) equations-of-state and opacity values were used. These simulations agree with the measured temporal X-ray signals from the DRDs and support the conclusion that X-rays in the forward direction are being attenuated by the mostly intact foil until after disassembly.

A clear illustration of the laser–foil interactions is revealed by following different zones through the hydrodynamic disassembly process of a 10-μm Cu foil in Fig. 7A. As the laser pulse arrives at the foil, the first micron of material is ablated from the front surface. The leading edge of this plasma comprising the first 100 nm of the foil is heated to ∼800 eV by the laser pulse. The remaining foil material is shock compressed to higher densities and pushed backward, until disassembling around the time of the peak of the laser pulse. The middle of the foil, material

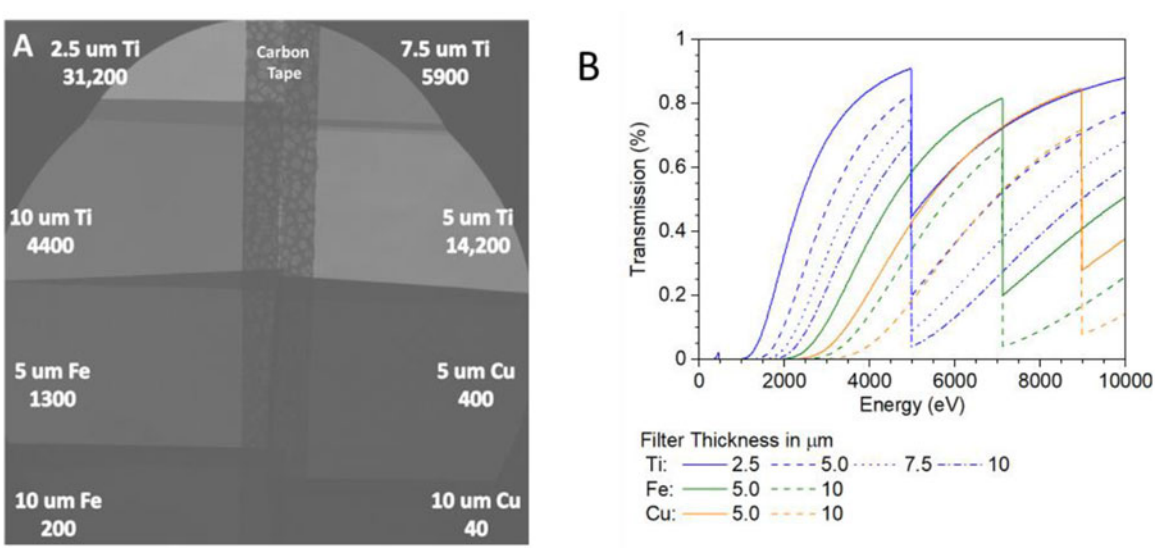

Figure 5. (A) X-ray image of the metal target filter with the filter type and average counts listed in each region. The image contrast and brightness has been adjusted for best visibility of each region. (B) X-ray transmission curves for Ti (blue), for Fe (green) and for Cu (orange). Note the strong K-edges in the chosen filter set and the small L edge for Ti at ∼500 eV.

https://doi.org/10.1017/lpb.2024.1 Published online by Cambridge University Press

between 4.0 and 4.1 μm, reaches temperatures of ∼60 eV from collisional heating by hotter electrons. The total mass density of the foil material and the simulated radiation flux from the front and back surface in Fig. 7B show that radiation in the backward direction begins almost immediately when the laser hits the foil. Radiation in the forward direction is not released until the foil has begun to disassemble and is significantly smaller in magnitude than the flux in the backward direction. Comparisons of simulations with different thicknesses of Cu in Fig. 7C show the expected trend towards more emission in the forward direction with thinner foils and slightly lower emission in the backward direction due to a smaller volume of high temperature plasma. Al, Ti and Fe foils exhibit all of the same general features, but comparisons of the magnitude of the radiation flux between materials in Fig. 7D do not match experiments or the Z^2 scaling from the inverse bremsstrahlung absorption coefficient. The timing of the simulated radiation pulses also deviates from experiments as the Al X-rays are simulated to show up the earliest as the lightest material disassembles the fastest, followed by Ti, Fe and then Cu. Experimental results measured Cu and Al X-ray pulses arriving at the detectors around the same time, followed a few nanoseconds later by Ti and then Fe.

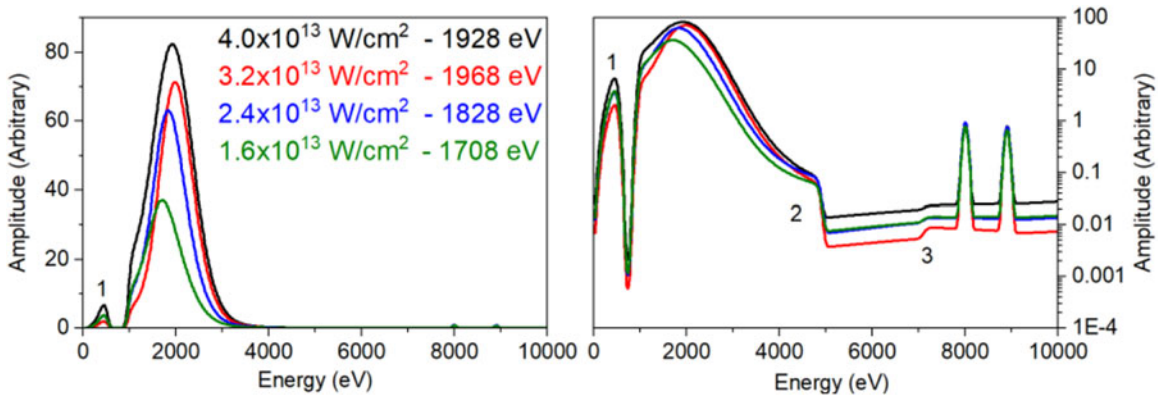

Figure 6. Spectral estimation with intensities of 1.6 × 10^{13} W/cm^2 (green), 2.4 × 10^{13} W/cm^2 (blue), 3.2 × 1013 W/cm^2 (red) and 4.0 × 10^{13} W/cm^2 J (black). The features marked by the numbers are artifacts of the chosen metal filters. The peaks at 8.5 and 8.9 keV are the locations of the Cu K-alpha and K-beta lines, respectively. These lines are significantly decreased from the original guess by the algorithm and are likely not present in the real experimental spectra.

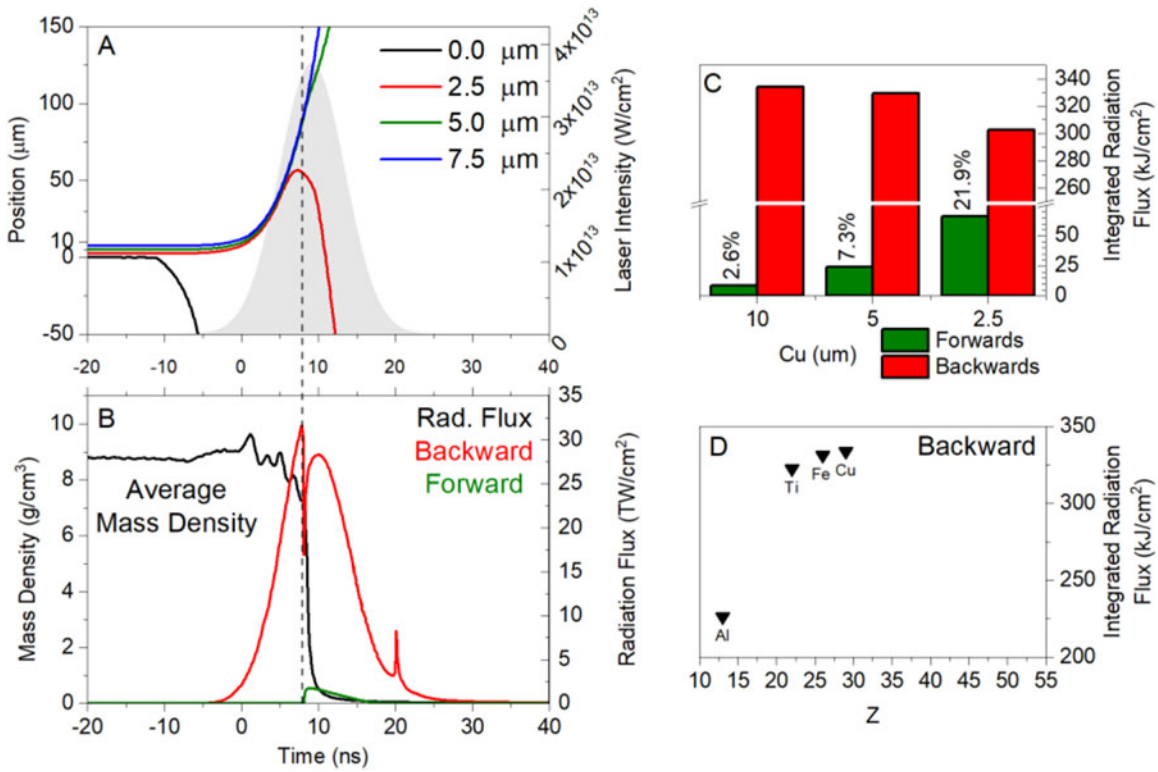

Figure 7. Results of HELIOS-CR simulations for Cu hydrodynamics irradiated by a 532-nm 5-J pulse with a 40-μm spot and a 10-ns FWHM at an intensity of 4 × 10^{13} W/cm^2. (A) Simulated foil motion from selected zones of a 10-μm-thick Cu foil with the laser pulse (grey). (B) On the same timescale, the mass density of the simulated foil and the simulated radiation flux in the forward direction (green) and radiation in the backward direction. (C) The simulated flux for different thicknesses of Cu compares favourably to experiment see Figure 4. (D) The simulated flux for different materials compares poorly with experiments, see Figure 2D.

https://doi.org/10.1017/lpb.2024.1 Published online by Cambridge University Press

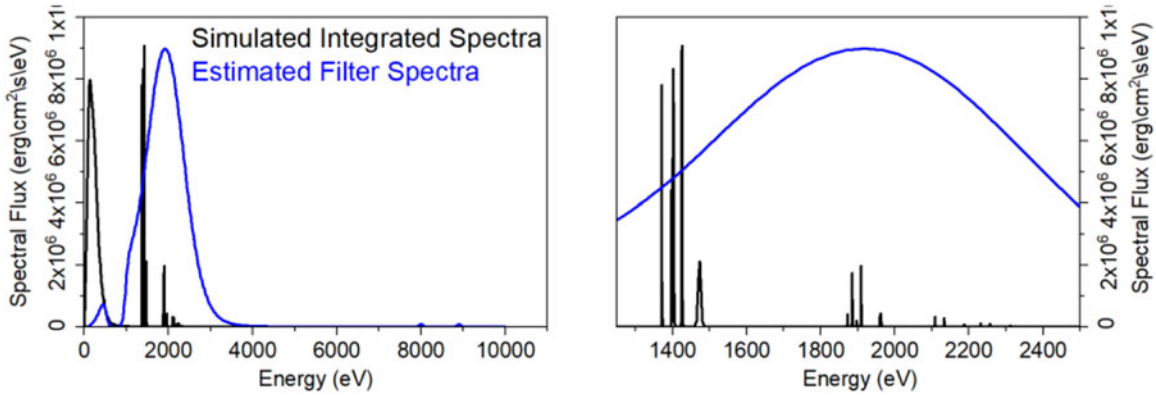

Figure 8. Simulated spectra from SPECT3D integrated over the full duration of the laser pulse exhibiting a black-body continuum from 0 to 800 eV and several Li-like Cu lines from 1.3 to 2.4 keV. Lines from He-like and H-like Cu atoms or Cu K-lines are not estimated to be emitted under these conditions. Spectra estimated from the filtered images at an equivalent laser intensity is scaled and shown for comparison in blue.

We simulated the spectra of the emitted radiation from the 5-μm-thick Cu foil using the output of the HELIOS-CR hydrodynamic data with SPECT3D (Ref. 44). We chose to use the non-local thermodynamic equilibrium K-line emission model for Cu which is native to the code. This atomic model includes the fully detailed states for H-like, He-like and Li-like Cu ions with the ground state for Be-like Cu ions. The time-integrated simulated X-ray spectra is shown in Fig. 8. At low energies, there is a black-body continuum from 0 to 800 eV and peaks at 143 eV. The group of emission lines from 1.3 to 2.4 keV is due to Li-like Cu^{26+} ions (Ref. 40). Using an estimated Boltzmann distribution and ionization energies tabulated by NIST (Ref. 40), the Li-like state comprises ∼4% of the plasma at a temperature of 800 eV. There is no emission of K-alpha, H-like or He-like lines around 8 keV in the simulated spectra. At an electron temperature of 800 eV, He-like Cu^{27+} and H-like Cu^{28+} comprise only 0.000098% and 0.000026% of the plasma using the same estimated Boltzmann distribution. We are not able to generate a high enough temperature with a laser intensity of 4×10^{13} W/cm^2 to produce Cu He-like and H-like ions in sufficient quantities to detect their characteristic X-rays. The simulated 1-D spectra roughly agree with the estimated spectra from the X-ray filtered imaging as the black-body emission is filtered out and there are no high energy lines. The simulated and estimated spectra do peak at different wavelengths, 1.4 keV vs. 1.9 keV, which may be due to emission from other ionized Cu species that are not included in the atomic model used by SPECT3D (Ref. 44). This also does not include the very real possibility of metal impurities or other absorbed elements contaminating the experimental spectra (Ref. 45).

Conclusion

We have built and characterized a modest intensity of 4×10^{13} W/cm^2, laser-produced plasma, soft X-ray source using a single 5-J, 8-ns (FWHM), 532-nm pulse on Al, Ti, Fe, SS-304, Cu and Sn foil targets. This work, in agreement with other studies (Refs 13, 20), has found that Cu has the largest X-ray yield for laser-produced plasma at these intensities. Foil targets introduce additional X-ray emission complications due to the hydrodynamic disassembly process compared to a solid cylinder (Refs 13, 14, 18, 19), or a flat solid target (Refs 20–23). X-ray emission begins with a material ablated from the front of the foils and is detected earlier on DRDs facing the front surface. X-rays reaching DRDs behind the foil are heavily attenuated by the foil until the hydrodynamic disassembly time with signals that are about 10 times smaller than DRDs facing the front surface. The ratio of forward/backward X-ray emission has been used to measure the ablation rate of the foils and suggests a thermal, boiling-like process with temperature of ∼0.6 eV. Spectral estimation of the emitted X-rays from Cu was calculated with an expectation–maximization algorithm by imaging eight filters with a Sophia X-ray CCD camera. The estimated spectra peaks at 2 keV with no X-rays observed beyond 4 keV. There is no evidence of Cu K-alpha lines or He-like and H-like emission. The intensity, timing and spectra of the X-rays compare favourably to simulations performed using HELIOS-CR.

For future experiments, we explore ways to increase the intensity of the laser pulse on the target by decreasing the spot size. Placing the final lens inside the vacuum and reducing the focal length by a factor of 3 would result in an increase in intensity by a factor of 9 from 4×10^{13} to 3.6×10^{14} W/cm^2. HELIOS-CR simulations with 5 μm Cu targets suggest this would increase our maximum electron temperature to 1400 eV and our X-ray flux by ∼10 times if the irradiated area is equal. Future work will include fielding a mica Bragg spectrometer with a spectral range up to 4 keV, collected on calibrated image plates to obtain X-ray dose as a function of energy. Once this is implemented, the image plates will be replaced with a microchannel plate gated X-ray imager.

Supplementary Material. The supplementary material for this article can be found at https://doi.org/10.1017/lpb.2024.1.

Data Availability Statement. Raw DRD and Sophia camera image data used to support the findings of this study are available from the corresponding author upon request. The HELIOS-CR simulation package is available from Prism Computational Sciences, Inc at www.prism-cs.com (Ref. 41).

Acknowledgements. The authors appreciate the support and scientific discussions with Joseph Strehlow, Sasi Palaniyappan and Cort Gautier. They would like to take the opportunity to thank Ross Roybal and Sharon Dominguez for their manufacturing and design support.

Author Contributions. **L. Tyler Mix**: Investigation (lead); formal analysis (lead); visualization (lead); writing – original draft (lead). **James A. Maslow**: Investigation (supporting); resources (lead). **M.A. Jaworski**: Conceptualization (supporting); writing – review and editing (supporting). **Joshua E. Coleman**: Conceptualization (lead); writing – review and editing (lead); supervision (lead).

Funding Statement. This work was supported by the U.S. Department of Energy at Los Alamos National Laboratory. Los Alamos National Laboratory is operated by Triad National Security, LLC, for the National Nuclear Security Administration of U.S. Department of Energy (Contract No. 89233218CNA000001).

Conflicts of Interest. The authors declare that there is no conflict of interest regarding the publication of this paper.

References

1. **Schwarz HJ and Hora H** (1969) Laser interaction and related plasma phenomena. In *Proceedings of the First Workshop*. Rensselaer Polytechnic Institute, Springer: Rensselaer Polytechnic Institute.
2. **Matthews DL, Campbell EM, Ceglio NM, Hermes G, Kauffman R, Koppel L, Lee R, Manes K, Rupert V, Slivinsky VW, Turner R and Ze F** (1983) Characterization of laser-produced plasma x-ray sources for use in x-ray radiography. *Journal of Applied Physics* **54**(8), 4260–4268.
3. **Back CA, Davis J, Grun J, Suter LJ, Landen OL, Hsing WW and Miller MC** (2003) Multi-keV x-ray conversion efficiency in laser-produced plasmas. *Physics of Plasmas* **10**(5), 2047–2055.
4. **Back CA, Grun J, Decker C, Suter LJ, Davis J, Landen OL, Wallace R, Hsing WW, Laming JM, Feldman U, Miller MC and Wuest C** (2001) Efficient multi-keV underdense laser-produced plasma radiators. *Physical Review Letters* **87**(27), 275003.
5. **Aoyama M, Yamakawa K, Akahane Y, Ma J, Inoue N, Ueda H and Kiriyama H** (2003) 0.85-PW, 33-fs Ti:sapphire laser. *Optics Letters* **28**(17), 1594–1596.
6. **Workman J, Cobble J, Flippo K, Gautier DC and Letzring S** (2008) High-energy, high-resolution x-ray imaging on the Trident short-pulse laser facility. *Review of Scientific Instruments* **79**(10), 10E905.
7. **Hill MP, Williams GJ, Zylstra AB, Stan CV, Lockard TE, Gumbrell ET, Rudd RE, Powell PD, Swift DC, McNaney JM, Galloudec KKL, Remington BA and Park H-S** (2021) High resolution >40 keV x-ray radiography using an edge-on micro-flag backlighter at NIF-ARC. *Review of Scientific Instruments* **92**(3), 033535.
8. **Landen OL, Farley DR, Glendinning SG, Logory LM, Bell PM, Koch JA, Lee FD, Bradley DK, Kalantar DH, Back CA and Turner RE** (2001) X-ray backlighting for the National Ignition Facility (invited). *Review of Scientific Instruments* **72**(1), 627–634.
9. **Bullock AB, Landen OL and Bradley DK** (2001) Relative x-ray backlighter intensity comparison of Ti and Ti/Sc combination foils driven in double-sided and single-sided laser configuration. *Review of Scientific Instruments* **72**(1), 686–689.
10. **Hollinger R, Bargsten C, Shlyaptsev VN, Kaymak V, Pukhov A, Capeluto MG, Wang S, Rockwood A, Wang Y, Townsend A, Prieto A, Stockton P, Curtis A and Rocca JJ** (2017) Efficient picosecond x-ray pulse generation from plasmas in the radiation dominated regime. *Optica* **4**(11), 1344–1349.
11. **Lureau F, Matras G, Chalus O, Derycke C, Morbieu T, Radier C, Casagrande O, Laux S, Ricaud S, Rey G, Pellegrina A, Richard C, Boudjemaa L, Simon-Boisson C, Baleanu A, Banici R, Gradinariu A, Caldararu C, Boisdeffre BD, Ghenuche P, Naziru A, Kolliopoulos G, Neagu L, Dabu R, Dancus I and Ursescu D** (2020) High-energy hybrid femtosecond laser system demonstrating 2 × 10 PW capability. *High Power Laser Science and Engineering* **8**, e43.
12. **Li W, Gan Z, Yu L, Wang C, Liu Y, Guo Z, Xu L, Xu M, Hang Y, Xu Y, Wang J, Huang P, Cao H, Yao B, Zhang X, Chen L, Tang Y, Li S, Liu X, Li S, He M, Yin D, Liang X, Leng Y, Li R and Xu Z** (2018) 339 J high-energy Ti:sapphire chirped-pulse amplifier for 10 PW laser facility. *Optics Letters* **43**(22), 5681–5684.
13. **Marzi S, Giulietti A, Giulietti D, Gizzi LA and Salvetti A** (2000) High brightness laser–plasma X-ray source at IFAM: Characterization and applications. *Laser and Particle Beams* **18**(1), 109–118.
14. **Labate L, Galimberti M, Giulietti A, Giulietti D, Gizzi LA, Tomassini P and Di Cocco G** (2002) A laser-plasma source for CCD calibration in the soft X-ray range. *Nuclear Instruments and Methods in Physics Research Section A: Accelerators, Spectrometers, Detectors and Associated Equipment* **495**(2), 148–153.
15. **Nishimura H** (2009) X-ray sources. In Eliezer S and Mima K (eds), *Applications of Laser-Plasma Interactions*. Boca Raton: CRC Press, 81–113.
16. **Zel'dovich YB and Raizer YP** (1967) *Physics of Shock Waves and High Temperature Hydrodynamic Phenomena*, Vol. 1. New York: Academic Press.
17. **Chen FF** (1974) *Introduction to Plasma Physics*. New York: Plenum Press.
18. **Labate L, Galimberti M, Giulietti A, Giulietti D, Gizzi LA and Numico R** (2002) Analysis of space-resolved X-ray spectra from laser plasmas. *Laser and Particle Beams* **20**(2), 223–226.
19. **Labate L, Galimberti M, Giulietti A, Giulietti D, Gizzi LA, Numico R and Salvetti A** (2001) Line spectroscopy with spatial resolution of laser–plasma X-ray emission. *Laser and Particle Beams* **19**(1), 117–123.
20. **Eidmann K and Kishimoto T** (1986) Absolutely measured x-ray spectra from laser plasmas with targets of different elements. *Applied Physics Letters* **49**(7), 377–378.
21. **Chaurasia S, Munda DS, Tripathi S, Gupta NK, Dhareshwar LJ and Tallents GJ** (2009) Effect of the laser focus position on characteristics of X-ray and ion emission from gold plasmas generated by a sub-nanosecond laser. *Nuclear Instruments and Methods in Physics Research Section B: Beam Interactions with Materials and Atoms* **267**(23), 3611–3616.
22. **Chaurasia S, Tripathi S, Ryc L and Dhareshwar LJ** (2011) Influence of laser focal position on X-ray and ion emission of copper plasma. *Nuclear Instruments and Methods in Physics Research Section A: Accelerators, Spectrometers, Detectors and Associated Equipment* **638**(1), 110–115.
23. **Chaurasia S, Tripathi S, Leshma P, Murali CG and Pasley J** (2013) Optimization of bremsstrahlung and characteristic line emission from aluminum plasma. *Optics Communications* **308**, 169–174.
24. **Gaeta CJ, Rieger H, Turcu ICE, Forber RA, Campeau SM, Cassidy KL, Powers MJ, Maldonado JR, French G, Naungayan J, Kelsey C, Hark P, Morris JH, Foster RM, Smith HI and Lim MH** (2002) High-power compact laser-plasma source for X-ray lithography. *Japanese Journal of Applied Physics* **41**(6S), 4111.
25. DARHT Facility: A Critical Component of Stockpile Stewardship. https://www.lanl.gov/science-innovation/science-facilities/DARHT/ (accessed 28 October 2022).
26. Continuum Powerlite Furie, discontinued. https://www.photonicsolutions.co.uk/upfiles/PowerliteFurieLDDatasheetLG07Dec17.pdf (accessed 30 September 2022).
27. **Labs T** Free Space Biased Detectors - DET10A2. https://www.thorlabs.com/newgrouppage9.cfm?objectgroup_id=1295&pn=DET10A2 (accessed 30 September 2022).
28. **Spielman RB, Ruggles LE, Pepping RE, Breeze SP, McGurn JS and Struve KW** (1997) Fielding and calibration issues for diamond photoconducting detectors. *Review of Scientific Instruments* **68**(1), 782–785.
29. **Kania DR, Pan L, Kornblum H, Bell P, Landen ON and Pianetta P** (1990) Soft x-ray detection with diamond photoconductive detectors. *Review of Scientific Instruments* **61**(10), 2765–2767.
30. **Turner RE, Landen OL, Bell P, Costa R and Hargrove D** (1999) Achromatically filtered diamond photoconductive detectors for high power soft x-ray flux measurements. *Review of Scientific Instruments* **70**(1), 656–658.
31. Diamond Radiation Detectors - CV Technologies. https://www.cvtechhardware.com/ (accessed 30 September 2022).
32. Sophia - XO. https://www.princetoninstruments.com/products/sophia-family/sophia-xo (accessed 5 August 2022).
33. Luxel Corp Standard Light Filters. https://luxel.com/products/filters/standard-filters/ (accessed 30 September 2022).
34. Goodfellow Foils. https://www.goodfellow.com/us/en-us/foil (accessed 30 September 2022).
35. **Hubbell JH and Seltzer SM** (2004) *Tables of X-Ray Mass Attenuation Coefficients and Mass Energy-Absorption Coefficients (Version 1.4)*. Gaithersburg, MD: National Institute of Standards and Technology.
36. **Gullikson E** X-Ray Interactions With Matter. https://henke.lbl.gov/optical_constants/ (accessed 8 August 2022).

37. **Henke BL, Gullikson EM and Davis JC** (1993) X-ray interactions: Photoabsorption, scattering, transmission, and reflection at E = 50-30,000 eV, Z = 1-92. *Atomic Data and Nuclear Data Tables* **54**(2), 181–342.
38. **Sidky EY, Yu L, Pan X, Zou Y and Vannier M** (2005) A robust method of x-ray source spectrum estimation from transmission measurements: Demonstrated on computer simulated, scatter-free transmission data. *Journal of Applied Physics* **97**(12), 124701.
39. **Duan X, Wang J, Yu L, Leng S and McCollough CH** (2011) CT scanner x-ray spectrum estimation from transmission measurements. *Medical Physics* **38**(2), 993–997.
40. **Kramida A, Ralchenko Y, Reader J** and NIST ASD Team NIST Atomic Specta Database. https://physics.nist.gov/asd (accessed 3 October 2022).
41. **MacFarlane JJ, Golovkin IE and Woodruff PR** (2006) HELIOS-CR – A 1-D radiation-magnetohydrodynamics code with inline atomic kinetics modeling. *Journal of Quantitative Spectroscopy and Radiative Transfer* **99**(1), 381–397.
42. **MacFarlane JJ, Golovkin IE, Mancini RC, Welser LA, Bailey JE, Koch JA, Mehlhorn TA, Rochau GA, Wang P and Woodruff P** (2005) Dopant radiative cooling effects in indirect-drive Ar-doped capsule implosion experiments. *Physical Review E* **72**(6), 066403.
43. **Bailey JE, Chandler GA, Slutz SA, Bennett GR, Cooper G, Lash JS, Lazier S, Lemke R, Nash TJ, Nielsen DS, Moore TC, Ruiz CL, Schroen DG, Smelser R, Torres J and Vesey RA** (2002) X-ray imaging measurements of capsule implosions driven by a Z-pinch dynamic hohlraum. *Physical Review Letters* **89**(9), 095004.
44. **MacFarlane J, Golovkin I and Woodruff P** (2003) SPECT3D imaging and spectral analysis suite. *Prism Computational Sciences Report No. PCS*.
45. **Ramey NB, Coleman JE, Hakel P, Morris HE, Colgan J, Barefield JE, Fontes CJ, Gilgenbach RM and McBride RD** (2021) Sodium tracer measurements of an expanded dense aluminum plasma from e-beam isochoric heating. *Physics of Plasmas* **28**(3), 033301.

https://doi.org/10.1017/lpb.2024.1 Published online by Cambridge University Press